Ehrig, K., et al., 2021, Staged formation of the supergiant Olympic Dam uranium deposit, Australia: Geology, v. 49, https://doi.org/10.1130/G48930.1

# Supplemental Material

## 1. Mine-scale maps of Cu, U, Pb grades

The 3-dimensional distribution of Cu-Pb-U was estimated using standard mining industry geostatistical techniques (i.e., ordinary and multiple indicator kriging, Rossi and Deutsch, 2014). Spatial modelling of Cu, U, Pb grades is supported by >1.8 million assayed drill core intervals (1-2.5 m long) from >12,000 diamond drill holes totalling >3 million meters in length (Wright et al., 2019). The deposit is discretised into ~20 million blocks varying in size from 5x10x5 to 30x30x15 m, depending on drill hole spacing; drill hole spacing varies within the resource outline from 20 m to 100 m. Cu-Pb-U grades are then estimated into the ~20 million blocks. Fig. 1 consists of depth slices through the 3D models of Cu, U and Pb distribution.

The U-Pb concentration estimates obtained here were used to calculate U/Pb ratios (by weight) from the resource estimates as a function of U concentration (see Fig. 2). U-Pb ages equivalent to these $U/Pb_{wt}$ estimates are given along the right-hand vertical axis in Fig. 2. These 'chemical' U-Th-Pb ages (also used in main text) were calculated using the general 'CHIME' equation (e.g., Cocherie and Legendre, 2007)

## 2. Analytical Methods

### 2.1 SEM imaging

Rock fragments from U ore samples and sulfide grains were cast in 1-inch epoxy mounts and polished with 0.3-micron alumina abrasive. Mineral images were acquired using an FEI Quanta 450 FEG Environmental Scanning Electron Microscope at Adelaide Microscopy, University of Adelaide.

### 2.2 U-Th-Pb isotope and elemental (major/trace element) analysis

Isotopic and chemical analyses of uraninites and of sulfide and hematite grain concentrates previously examined by SEM were done by laser ablation ICP-MS at the CODES Analytical Laboratories, University of Tasmania, Hobart. In all cases, laser micro-sampling was carried out with Applied Spectra Resolution laser ablation systems which incorporate a 193 nm ArF excimer laser source. For uraninite and hematite, a Resolution LR (with a CompexPro 110 ~20 ns pulse width laser) coupled to an Agilent 7900 ICP-MS was used. Sulfides were

ablated using a Resolution SE (with an ATL ATLEX 300, ~5 ns pulse width) coupled to an Agilent 7700 ICP-MS. The S-155 ablation chamber from Laurin Technic was used throughout. The ICP-MS instruments were tuned for maximum sensitivity and low oxide production ($^{232}Th^{16}O/^{232}Th$ <0.002). Ablations were carried out under helium (0.35 l/min), followed by transfer of the ablated material to the mass spectrometer in high-purity argon (~1.05 l/min). Nitrogen gas (~1.5 ml/min) was added to the gas stream after the ablation cell to improve sensitivity, and a signal smoothing device ('squid') was used as part of the transfer line.

*In situ* U-Th-Pb isotope analyses of uraninite were done with a 10 μm laser spot (5 Hz, ~2.0 J/cm$^2$ fluence) and included the masses $^{202}Hg$, $^{204}Pb$, $^{206}Pb$, $^{207}Pb$, $^{208}Pb$, $^{232}Th$, $^{235}U$, $^{238}U$ and $^{67}Cu$. The detector mode for $^{206}Pb$ and $^{238}U$ was forced to analog mode to avoid non-linearity issues with possible changes in detection modes during ablation, a common issue in uraninite ablated with a 10 μm spot size. Where needed, a modern $^{238}U/^{235}U$ of 137.82 was used. Counting times were 5 ms for $^{202}Hg$, $^{206}Pb$, $^{208}Pb$ and $^{232}Th$ those for $^{204}Pb$, $^{207}Pb$ and $^{235}U$ were 20, 10 and 10 ms, respectively. Following a 30 second 'gas blank', targets were ablated for 20 seconds. A concordant uraninite sample (Kintyre U deposit, Western Australia, ~840 Ma, Cross et al., 2011) was measured in duplicate at the start and end of each session, and after every ~15 unknowns. Time-resolved results for this sample were compiled to define corrections for downhole elemental fractionation and ICP-MS drift (e.g., Paton et al., 2010). Pb isotope mass bias and drift were monitored and corrected using the NIST610 glass. All data reduction was done using an in-house MS Excel spreadsheet, with error propagation following (Horstwood et al., 2016; Thompson et al., 2016). Concordia diagrams were constructed using Isoplot 3.7 or 4.08 (Ludwig, 2008).

Concentrations of 41 elements in uraninite were measured in separate runs, using NIST610 glass as a reference sample. Uranium concentrations previously determined by EDS-SEM were used as internal standard. The masses analysed are: $^{24}Mg$, $^{27}Al$, $^{29}Si$, $^{31}P$, $^{39}K$, $^{43}Ca$, $^{49}Ti$, $^{51}V$, $^{55}Mn$, $^{57}Fe$, $^{59}Co$, $^{60}Ni$, $^{65}Cu$, $^{66}Zn$, $^{89}Y$, $^{93}Nb$, $^{95}Mo$, $^{137}Ba$, $^{139}La$, $^{140}Ce$, $^{141}Pr$, $^{146}Nd$, $^{147}Sm$, $^{151}Eu$, $^{157}Gd$, $^{159}Tb$, $^{162}Dy$, $^{165}Ho$, $^{166}Er$, $^{169}Tm$, $^{172}Yb$, $^{175}Lu$, $^{178}Hf$, $^{181}Ta$, $^{182}W$, $^{197}Au$, $^{202}Hg$, $^{204}Pb$, $^{206}Pb$, $^{207}Pb$, $^{208}Pb$, $^{232}Th$, $^{235}U$, and $^{238}U$.

*In situ* Pb isotope and elemental compositions of Cu sulfide minerals (chalcopyrite, bornite, chalcocite) and hematite were determined using the using the instrumentation described above. Data were acquired using a 30 µm laser spot (5 Hz, fluence ~ 3.2-3.5 J/cm$^2$ for hematite, 6-8.7 J/cm$^2$ for sulfides). Elemental concentrations in Cu sulfides were calculated using stoichiometric Fe (chalcopyrite, bornite) or Cu (chalcocite) as internal standards, and the reference samples STDGL3 (a synthetic glass doped with Fe- and Zn sulfide powders, Belousov et al., 2015) and GSD-1G (basalt glass, Jochum et al., 2005). Elemental concentrations in hematite analyses were quantified using stoichiometric Fe as internal and GSD-1G as external standard. GSD-1G was also used to check the accuracy of the measured Pb isotope ratios and to constrain $^{238}U/^{206}Pb$, employing the U-Pb isotope composition reported in the GeoREM data base (http://georem.mpch-mainz.gwdg.de). Data reduction was done using the LADR software (www.norsci.com).

**3. Interpretation of Pb isotope results for Cu sulfides**

The analysed Cu sulfide minerals have wide ranges of U (chalcopyrite 0-20000 ppm, bornite 0-4300 ppm, chalcocite 0-1950 ppm) and Pb (chalcopyrite <1 to 8000 ppm, bornite 1-19000 ppm, chalcocite 0-190000 ppm); these data are not included here but are available from the senior author (KE). Th/U is mostly <0.1 although bornite has rare Th-rich domains in which Th/U is up to 200. Pb isotope ratios also vary widely, from those typical of common Pb to highly radiogenic compositions (e.g., $^{206}Pb/^{204}Pb$ >7000 in chalcopyrite and >10000 in bornite). In $^{207}Pb/^{204}Pb$ - $^{206}Pb/^{204}Pb$ diagrams, the data for the three minerals form scattered but linear trends with slopes of 0.0640, 0.0659 and 0.0673 (chalcopyrite, bornite, chalcocite, respectively; the most radiogenic points for bornite and chalcocite excluded). On $^{207}Pb/^{206}Pb$ – $^{238}U/^{206}Pb$ diagrams (the Tera-Wasserburg condordia plot), the vast majority of the data points plots on the low-U/Pb side of the concordia line. This effect is particularly obvious at low $^{207}Pb/^{206}Pb$ (<0.2) and indicates that radiogenic Pb in these analyses is largely 'unsupported' by sulfide U contents. Exceptions exist and are related to strongly elevated U concentrations, presumably from small inclusions of U minerals.

In contrast to the Cu sulfide minerals, the analysed hematite grains have higher U/Pb ratios and plot largely on the high-U/Pb side of the Tera-Wasserburg concordia line, indicating that radiogenic Pb in these analyses is 'supported' by hematite U contents, i.e., that radiogenic Pb ingrowth is likely to have been cumulative at most analysed sites. Pb isotope compositions cover a very large range. On a $^{207}Pb/^{204}Pb$ - $^{206}Pb/^{204}Pb$ diagram, the data form a well-defined

trend with a slope of 0.0983, equivalent to a Pb-Pb isochron age near 1.59 Ga, identical to the oldest uraninite ages reported from Olympic Dam (e.g. Apukhtina et al., 2017).

Unsupported radiogenic Pb in sulfide minerals is known from many U deposits where uraninite/pitchblende has released highly radiogenic Pb subsequently captured in authigenic sulfides. Examples include the radiogenic galena at the Jabiluka and Shea Creek deposits (Gulson and Mizon, 1980; Kister et al., 2004). Mixing of radiogenic Pb of this type with less radiogenic Pb (including ambient common Pb from older sulfides) will produce linear trends on various Pb-Pb isochron diagrams (e.g., Fig.4A inset, main text). Scatter on these trends may reflect the presence of radiogenic Pb expelled from parental U minerals of different ages, or at different times. Additional sources of scatter include mineral impurities and analytical issues at low $^{207}Pb$ concentrations. Some very low $^{207}Pb/^{206}Pb$ ratios (<0.05) may reflect the presence in some sulfide grains of excess $^{206}Pb$ from $^{234}U$ loss in radiation-damaged U minerals. However, most measured $^{207}Pb/^{206}Pb$ are >0.06 and the vast majority of the sulfide analyses cluster in well-defined trends. The slopes of such trends can be converted to conventional $^{207}Pb$-$^{206}Pb$ isochron ages of 740, 803 and 846 Ma for chalcopyrite, bornite and chalcocite, respectively, according to the following equation:

**Eq.1** $$^{207}Pb^*/^{206}Pb^* = (1/137.82) \times [(e^{\lambda bt} - 1) / (e^{\lambda at} - 1)]$$

where $^{207}Pb^*/^{206}Pb^*$ is the slope of the Pb-Pb isochron and identical to the $^{207}Pb/^{206}Pb$ ratio of the radiogenic Pb component that provides one endmember of the Pb-Pb isotopic trend (* denotes 'radiogenic'); $\lambda_a$ and $\lambda_b$ are the decay constants for $^{238}U$ ($0.155125 \times 10^{-9}$/yr) and $^{235}U$ ($0.98485 \times 10^{-9}$/yr), respectively; 137.82 is the modern $^{238}U/^{235}U$ (Hiess et al., 2012); and t is the Pb-Pb isochron age (Faure, 1986).

However, interpretation of such Pb isotope trends as secondary Pb-Pb isochrons assumes that the radiogenic Pb compositions are supported by U (or were supported by suitable U/Pb ratios until geologically recent time). If the radiogenic Pb is unsupported Pb incorporated into its present host minerals in the distant geological past, an interpretation based on cumulative Pb ingrowth will result in ages that are too old. In the extreme case, this unsupported radiogenic Pb may be 'instantaneous Pb' transferred from their parental U minerals soon after its formation. The age of this instantaneous Pb can be calculated as

**Eq.2** $t = (1/( \lambda_b - \lambda_a)) \times \ln[(137.82 \times {}^{207}Pb^*/{}^{206}Pb^* \times \lambda_a)/ \lambda_b]$

where t is the age of 'instantaneous' radiogenic Pb ingrowth in a U-rich mineral (Faure, 1986).

For the Cu sulfide Pb isotope trends described above, with slopes of 0.0640-0.0673, eq.2 yields model ages of 396 to 457 Ma for the parental U minerals, considerably younger than the conventional sulfide Pb-Pb isochron ages (740-846 Ma). The slopes of Pb isotope trends controlled by unsupported radiogenic Pb are more generally described with the following equation:

**Eq.3** ${}^{207}Pb^*/{}^{206}Pb^* = (1/137.82) \times [(e^{\lambda bt1} - e^{\lambda bt2}) / (e^{\lambda at1} - e^{\lambda at2})]$

where $t_1$ and $t_2$ are the start and end points of radiogenic Pb ingrowth producing ${}^{207}Pb^*/{}^{206}Pb^*$ within a U-rich mineral; $t_2$ is identical to the time 'supported' Pb* is transferred to a U-poor new carrier to become 'unsupported' Pb* (Faure, 1986).

Instantaneous Pb* is produced when $t_2 = t_1$ (see Eq.2) and fully supported Pb* is produced where $t_2 = 0$, i.e. ingrowth stops at the present. A convenient way to map the distribution of ${}^{207}Pb^*/{}^{206}Pb^*$ generated as a result of varying $t_1$ and $t_2$ is the $t_1$-$t_2$ diagram shown in Fig. 4B and below (Fig. SM1). In this diagram, contour lines of constant ${}^{207}Pb^*/{}^{206}Pb^*$ are shown between the x-axis (=$t_1$, eq.1) and a diagonal line with slope 1. The former is the locus of 'cumulative' radiogenic Pb, i.e., U-Pb systems that were closed until the present; by definition $t_2$=0. The line with slope 1 is the locus of instantaneous radiogenic Pb (eq.2, $t_2$=$t_1$).

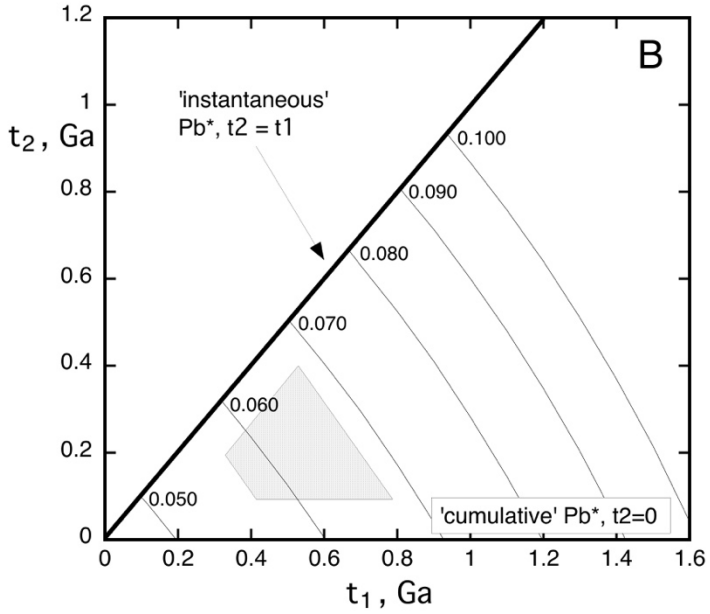


Fig. SM1. Relationship between $^{207}Pb/^{206}Pb^*$ (diagonal dashed trends), $t_1$ (the age of U mineral formation, x-axis) and $t_2$ (the age of Pb* release from its parental U mineral, y-axis, for details see item 3). $^{207}Pb/^{206}Pb^*$ ratios for Cu sulfides centered on 0.006-0.07 (shaded polygon) imply a major period of U mineralization in the late Neoproterozoic-Cambrian, followed by transfer of ingrown Pb* as well as pyrite (not shown) some tens to hundreds of million years later.

In this diagram, measured $^{207}Pb^*/^{206}Pb^*$ can be used to constrain $t_1$ and $t_2$. For example, a U mineral formed at $t_1$=1 Ga would generate instantaneous Pb* with $^{207}Pb^*/^{206}Pb^* = 0.1055$. Subsequent ingrowth produces primarily $^{206}Pb^*$, gradually driving the accumulated $^{207}Pb^*/^{206}Pb^*$ towards the x-axis: $^{207}Pb^*/^{206}Pb^*$ will be 0.0866 at $t_2$=500 Ma and 0.0777 at $t_2$=200 Ma.

The Cu sulfide minerals analyzed here have highly variable $^{207}Pb/^{206}Pb$ (Fig. 4A) but their average $^{207}Pb^*/^{206}Pb^*$ratios inferred from y-axis intercepts ($^{204}Pb/^{206}Pb = 0$, Fig. 4a inset) are in the range 0.0584 to 0.0669. This range constrains $t_1$ and $t_2$ for these radiogenic Pb's to the area approximated by the shaded polygon in Fig. SM1. The position of this polygon assumes (i) that Pb* in the sulfides is not purely instantaneous Pb* (as this would generate very little Pb), and (ii) that $t_2$ is not 0. Although these assumptions are to some extent arbitrary, it seems clear that in the case of the Olympic Dam Cu sulfides, $t_1$ is in the period 800 to 400 Ma and that exsolution of Pb* ($t_2$) occurred in the Phanerozoic. These age estimates imply that radiogenic Pb in Cu sulfides from across the deposit originated from late Neoproterozoic to Cambrian/Ordovician U mineralization. Remnants of this U mineralization event may be

preserved in the form of the ca. 0.6-0.5 Ga uraninite ages reported here (Fig. 3A). Formation of the current sulfide mineral hosts of this Pb must postdate the late Neoproterozoic to Cambrian/Ordovician U mineralization event. Uptake of radiogenic Pb into Cu sulfides may have involved modification of older Cu sulfide minerals (e.g., Ciobanu et al., 2017), providing an explanation for the presence of common Pb in these Cu sulfides.

**References**


Apukhtina, O. B., Kamenetsky, V. S., Ehrig, K., Kamenetsky, M. B., Maas, R., Thompson, J., McPhie, J., Ciobanu, C. L., and Cook, N. J., 2017, Early, deep magnetite-fluorapatite mineralization at the Olympic Dam Cu-U-Au-Ag deposit, South Australia: Economic Geology, v. 112, p. 1531-1542, https://doi.org/10.5382/econgeo.2017.4520.

Belousov, I., Danyushevsky, L., Olin, P. H., Gilbert, S., and Thompson, J., STDGL3 - a new calibration standard for sulphide analysis by LA-ICP-MS, *in* Proceedings Goldschmidt Prague, Czech Republic, 2015.

Ciobanu, C. L., Cook, N. J., and Ehrig, K., 2017, Ore minerals down to the nanoscale: Cu-(Fe)-sulphides from the iron oxide copper gold deposit at Olympic Dam, South Australia: Ore Geology Reviews, v. 81, p. 1218-1235, https://doi.org/10.1016/j.oregeorev.2016.08.015.

Cocherie, A., and Legendre, O., 2007, Potential minerals for determining U–Th–Pb chemical age using electron microprobe: Lithos, v. 93, p. 288-309, https://doi.org/10.1016/j.lithos.2006.03.069.

Cross, A., Jaireth, S., Rapp, R., and Armstrong, R., 2011, Reconnaissance-style EPMA chemical U–Th–Pb dating of uraninite: Australian Journal of Earth Sciences, v. 58, p. 675-683, https://doi.org/10.1080/08120099.2011.598190.

Faure, G., 1986, Principles of Isotope Geology, New York, John Wiley and Sons, 589 p.:

Gulson, B. L., and Mizon, K. J., 1980, Lead isotope studies at Jabiluka, *in* Ferguson, J., and Goleby, A., eds., Uranium in the Pine Creek Geosyncline: Vienna, International Atomic Energy Agency, p. 439-456.

Hiess, J., Condon, D. J., McLean, N., and Noble, S. R., 2012, $^{238}U/^{235}U$ Systematics in Terrestrial Uranium-Bearing Minerals: Science, v. 335, p. 1610-1614, 10.1126/science.1215507.

Horstwood, M. S. A., Kosler, J., Gehrels, G., Jackson, S. E., McLean, N. M., Paton, C., Pearson, N. J., Sircombe, K., Sylvester, P., Vermeesch, P., Bowring, J. F., Condon, D. J., and Schoene, B., 2016, Community-derived standards for LA-ICP-MS U-(Th-)Pb geochronology - uncertainty propagation, age interpretation and data reporting: Geostandards and Geoanalytical Research, v. 40, p. 311-332, https://doi.org/10.1111/j.1751-908X.2016.00379.x.

Jochum, K., Willbold, M., Raczek, I., Stoll, B., and Herwig, K., 2005, Chemical characterisation of the USGS reference glasses GSA-1G, GSC-1G, GSD-1G, GSE-1G, BCR-2G, BHVO-2G and BIR-1G using EPMA, ID-TIMS, ID-ICP-MS and LA-ICP-MS: Geostandards and Geoanalytical Research, v. 29, p. 285-302, https://doi.org/10.1111/j.1751-908X.2005.tb00901.x.

Kister, P., Cuney, M., Golubev, V. N., Royer, J.-J., Le Carlier De Veslud, C., and Rippert, J.-C., 2004, Radiogenic lead mobility in the Shea Creek unconformity-related uranium deposit (Saskatchewan, Canada): migration pathways and Pb loss quantification:

Comptes Rendus Geoscience, v. 336, p. 205-215, https://doi.org/10.1016/j.crte.2003.11.006.

Ludwig, K. R., 2008, User's manual for Isoplot 3.70: A geochronological toolkit for Microsoft Excel, Berkeley, CA: University of California, Berkeley Geochronological Center Special Publication. .

Paton, C., Woodhead, J. D., Hellstrom, J. C., Hergt, J. M., Greig, A., and Maas, R., 2010, Improved laser ablation U-Pb zircon geochronology through robust downhole fractionation correction: Geochemistry, Geophysics, Geosystems, v. 11, https://doi.org/10.1029/2009gc002618.

Rossi, M. E., and Deutsch, C. V., 2014, Mineral Resource Estimation:, Dordrecht, Springer Netherlands.

Thompson, J., Meffre, S., Maas, R., Kamenetsky, V., Kamenetsky, M., Goemann, K., Ehrig, K., and Danyushevsky, L., 2016, Matrix effects in Pb/U measurements during LA-ICP-MS analysis of the mineral apatite: Journal of Analytical Atomic Spectrometry, v. 31, p. 1206-1215, 10.1039/C6JA00048G.

Wright, M., Clarke, D., Badenhorst, C., and O'Connell, S., Simple solutions for solving complex problems – combining MIK with OK estimation techniques at Olympic Dam, *in* Proceedings International Mining Geology Conference 2019, Volume 8/2019, Australasian Institute of Mining and Metallurgy, p. 198-209.